



Cite this: *J. Mater. Chem. A*, 2022, **10**, 10692

Na- β -Al₂O₃ stabilized Fe₂O₃ oxygen carriers for chemical looping water splitting: correlating structure with redox stability†

Nur Sena Yüzbasi, ^a Andac Armutlulu, ^a Thomas Huthwelker, ^b Paula M. Abdala ^{*a} and Christoph R. Müller ^{*a}

Chemical looping is an emerging technology to produce high purity hydrogen from fossil fuels or biomass with the simultaneous capture of the CO₂ produced at the distributed scale. This process requires the availability of stable Fe₂O₃-based oxygen carriers. Fe₂O₃-Al₂O₃ based oxygen carriers exhibit a decay in the H₂ yield with cycle number, due to the formation of FeAl₂O₄ that possesses a very low capacity for water splitting at typical operating conditions of conventional chemical looping schemes (700–1000 °C). In this study, the addition of sodium (*via* a sodium salt) in the synthesis of Fe₂O₃-Al₂O₃ oxygen carriers was assessed as a means to counteract the cyclic deactivation of the oxygen carrier. Detailed insight into the oxygen carrier's structure was gained by combined X-ray powder diffraction (XRD), X-ray absorption spectroscopy (XAS) at the Al, Na and Fe K-edges and scanning transmission electron microscopy/energy-dispersive X-ray spectroscopy (STEM/EDX) analyses. The addition of sodium prevented the formation of FeAl₂O₄ and stabilized the oxygen carrier *via* the formation of a layered structure, Na- β -Al₂O₃ phase. The material, *i.e.* Na- β -Al₂O₃ stabilized Fe₂O₃, showed a stable H₂ yield of ca. 13.3 mmol g⁻¹ over 15 cycles.

Received 8th December 2021
Accepted 11th April 2022

DOI: 10.1039/d1ta10507h
rsc.li/materials-a

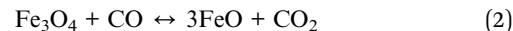
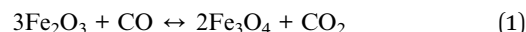
Introduction

Hydrogen is an emerging energy carrier with potential applications in the transport, industry and power sectors as a fuel that yields water vapour as the only combustion product. If produced sustainably, H₂ has the potential to become a near-zero emissions energy carrier, hence reducing energy-related CO₂ emissions.^{1–3} Currently, the majority of H₂ is produced from natural gas *via* steam methane reforming (SMR) without carbon dioxide capture, which is an energy intensive process and emits a significant amount of CO₂.^{3,4} In addition, further energy-intensive purification steps are required to obtain H₂ of sufficiently high purity allowing its use in polymer electrolyte membrane fuel cells (PEMFC).^{5,6} Hence, for H₂ to become an energy carrier in a sustainable framework, it must be produced in an efficient and sustainable manner, *i.e.* from renewable sources or with CO₂ capture.^{7,8}

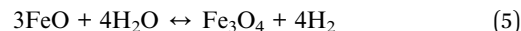
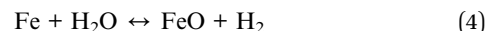
A chemical looping (CL) scheme based on the cyclic redox reactions of iron oxide/iron offers the possibility to produce high purity H₂ with inherent CO₂ capture (Fig. 1a).^{7–14} This process could be operated using different reducing gases such

as CO, synthesis gas (produced by biomass gasification) or natural gas.^{15,16} For instance, CO is used to reduce Fe₂O₃ to lower oxidation states (ideally to metallic Fe which gives the highest H₂ yield), following reactions (1)–(3). During Fe₂O₃ reduction, a pure stream of CO₂ is obtained readily through the condensation of water vapour. The oxidation of metallic Fe with steam produces H₂ (water splitting reactions (4) and (5)) of high purity.¹⁷ To close the cycle, Fe₃O₄ is oxidized to Fe₂O₃ in air (reaction (6)).

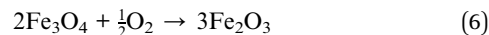
Reduction of iron oxide in CO



Oxidation in steam



Oxidation in air



^aLaboratory of Energy Science and Engineering, ETH Zurich, Leonhardstrasse 27, 8092, Zurich, Switzerland. E-mail: abdala@ethz.ch; muelchri@ethz.ch

^bSwiss Light Source, Paul Scherrer Institut, 5232, Villigen PSI, Switzerland

† Electronic supplementary information (ESI) available. See <https://doi.org/10.1039/d1ta10507h>



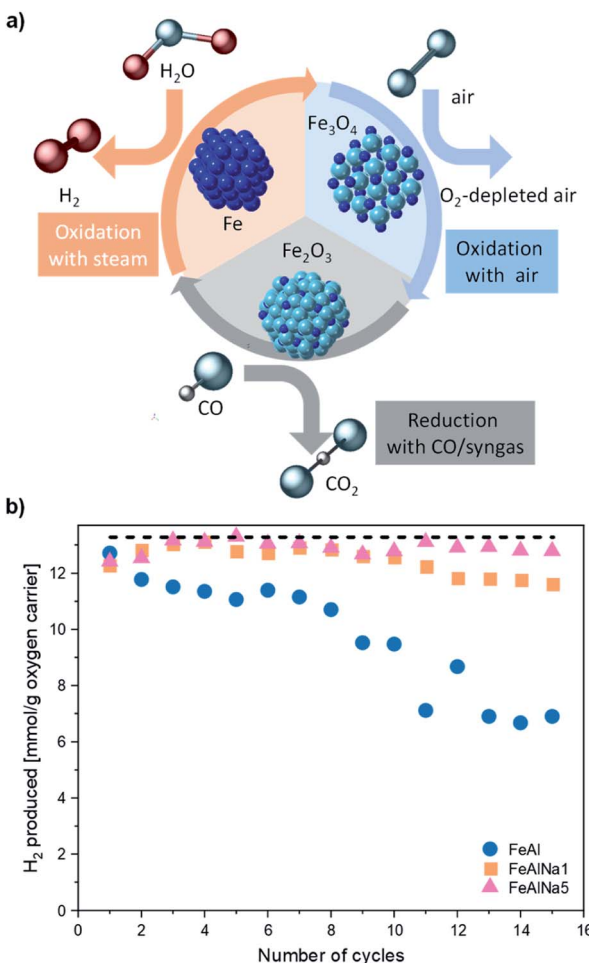


Fig. 1 (a) Schematic of the Fe₂O₃-Fe based chemical looping process for the production of H₂ using a synthesis gas (H₂ and CO) as the fuel. (b) H₂ yield as a function of cycle number for FeAl, FeAlNa1 and FeAlNa5. The redox experiments were performed at 800 °C in a packed-bed reactor using 10 vol% CO in N₂ for reduction and 23 vol% H₂O in N₂ followed by 5 vol% O₂ in N₂ for re-oxidation. The dashed horizontal line represents the theoretically expected H₂ yield (13.3 mmol g⁻¹) for an oxygen carrier that contains 80 wt% Fe₂O₃.

Owing to its favourable thermodynamics iron oxide is one of the most attractive oxygen carriers for the chemical-looping-based production of hydrogen.^{7-11,13,17-27} However, pure Fe₂O₃ shows a rapid decay in its H₂ yield with number of redox cycles owing to sintering.¹⁷ Sintering leads to an appreciable decrease in the reduction rate of iron oxide, which results in an incomplete reduction and in turn a low H₂ yield in the subsequent re-oxidation step.^{7,27,28} To mitigate deactivation by sintering, strategies based on the addition of a high Tammann temperature stabilizing oxide, *e.g.* Al₂O₃,^{7,10,22,26,29} SiO₂,^{7,9} TiO₂,³⁰ CeO₂,¹⁴ MgAl₂O₄^{21,31} and ZrO₂,^{13,23,27} have been proposed. Indeed, these oxides have shown to increase the stability of iron based oxygen carriers over multiple cycles by reducing FeO_x/Fe particle sintering.²³ Among the investigated oxides, Al₂O₃ is particularly interesting owing to its relatively low cost, high Tammann temperature of ~885 °C and high mechanical resistance.³²⁻³⁴ However, Al₂O₃ can react with iron oxide forming the spinel

phase FeAl₂O₄ (hercynite) which leads to a decay in the H₂ yield due to the limited capacity of FeAl₂O₄ to split water at the typical operating conditions of conventional CL (700–1000 °C).^{10,22,26,35} Hydrogen production using iron aluminate-based materials has been proposed for solar driven thermochemical cycles that cycles between spinel iron based solid solutions through an oxygen vacancy mediated mechanism; however, this is limited to high steam-to-hydrogen ratios and the H₂ capacity does not exceed 0.5 mmol H₂ per g FeAl₂O₄.³⁶⁻³⁸

Approaches to prevent the formation of FeAl₂O₄ during redox operation have included the addition of alkali or alkali earth metal oxides to the oxygen carrier, yet the mechanisms behind the mitigation of FeAl₂O₄ formation remains elusive.^{23,34,39} In particular, the effect of the addition of sodium on the redox performance of Fe₂O₃-Al₂O₃ based oxygen carriers is controversially discussed and the underlying mechanisms at the atomic scale that would explain the improved macroscopic redox performance of such oxygen carriers are currently not well understood. For instance, a previous study proposed that formulations based on Fe₂O₃, Al₂O₃, Na₂O and/or MgO could potentially hinder the formation of FeAl₂O₄ by forming NaAlO₂ or MgAl₂O₄ phases that are thermodynamically more stable.³¹ Indeed, X-ray powder diffraction (XRD) analysis confirmed the presence of NaAlO₂ and MgAl₂O₄ phases in the two studied oxygen carriers with compositions Na : Al : Fe = 0.25 : 0.25 : 0.50 and Na : Mg : Fe : Al = 0.20 : 0.15 : 0.28 : 0.37 (molar ratios). However, it was found that only MgAl₂O₄ effectively hindered the formation of inactive FeAl₂O₄ while NaAlO₂ only partially prevented its formation. This was explained by the gradual replacement of Al³⁺ by Fe³⁺ in NaAlO₂ (NaAl_{1-y}Fe_yO₂) during redox cycling leading to the formation of free Al₂O₃ that subsequently reacts with FeO_x to form FeAl₂O₄. A further study found that the addition of sodium in concentrations below 5 wt% stabilizes the reactivity of Fe₂O₃, yet the structure of the oxygen carriers was not studied in detail.^{20,40} Typically, X-ray powder diffraction (XRD) has been applied to identify the phases present in the oxygen carrier, however, this analysis fails at describing the local structure of the materials and it is insensitive to amorphous phases and phases in low concentration. Thus, the fine structural features of Na-modified Fe₂O₃-Al₂O₃ oxygen carriers remain elusive.

As discussed above, a difficulty in improving our understanding of the effect of the addition of sodium to Fe₂O₃-Al₂O₃ on its redox behaviour is the lack of knowledge of the atomic-scale structure of these materials. Thus, this work aims at shedding light on the structure-performance relationships of sodium modified Fe₂O₃-Al₂O₃ oxygen carriers for H₂-production by addressing the following questions: (i) how is the atomic scale structure of Fe₂O₃-Al₂O₃ based oxygen carriers modified by the addition of Na? (ii) what is the Na, Al and Fe environment in the oxygen carrier? and (iii) how does the redox performance relate to the oxygen carriers' structure? To address these questions we performed a detailed structural and redox analysis of sodium modified Fe₂O₃-Al₂O₃ and a sodium free benchmark utilizing XRD and X-ray absorption spectroscopy (XAS) data at the Fe, Al and Na K-edges.



Experimental

Synthesis of the oxygen carriers

$\text{Fe}_2\text{O}_3:\text{Al}_2\text{O}_3$ and Na-modified $\text{Fe}_2\text{O}_3:\text{Al}_2\text{O}_3$ oxygen carriers were synthesized using a sol-gel method²² with the following compositions: (i) Fe : Al molar ratio: 0.66 : 0.34 (75 wt% Fe_2O_3 , 25 wt% Al_2O_3), referred to as FeAl; (ii) Na : Fe : Al = 0.02 : 0.66 : 0.32 (76 wt% Fe_2O_3 , 23 wt% Al_2O_3 , 1 wt% Na_2O), referred to as FeAlNa1; and (iii) Na : Fe : Al 0.11 : 0.64 : 0.25 (76 wt% Fe_2O_3 , 19% wt% Al_2O_3 and 5 wt% Na_2O), referred to as FeAlNa5, (Table S1†). In a typical synthesis, aluminum isopropoxide ($\text{Al}(\text{OCH}(\text{CH}_3)_2)_3$, purity ≥ 98 wt%) was mixed with water and the mixture was hydrolysed for two hours at 75 °C under constant stirring. Nitric acid was used to peptize the slurry. The required amount of the iron and sodium precursors, iron nitrate ($\text{Fe}(\text{NO}_3)_3 \cdot 9\text{H}_2\text{O}$, purity ≥ 98 wt%) and sodium nitrate (NaNO_3 , purity ≥ 99 wt%) respectively, were mixed with water to obtain a 1 M solution that was added subsequently to the slurry and refluxed for 12 h at 90 °C. The molar ratio of $\text{Al}^{3+} : \text{H}_2\text{O} : \text{H}^+$ was fixed to 0.5 : 50 : 0.07. The resulting gel was dried at 100 °C overnight to remove the solvents. A xerogel was obtained after calcination at 900 °C for 2 hours. The calcined materials were crushed and sieved to a particle size range of 300–425 µm for further characterization.

Reference materials for structural characterization

The following reference materials for XAS analysis were synthesized. Na- β - Al_2O_3 , with a molar ratio of Na : Al = 1 : 11 ($\text{NaAl}_{11}\text{O}_{17}$, $P6_3/mmc$ space group³⁹) was synthesized by mixing stoichiometric amounts of γ - Al_2O_3 and Na_2CO_3 followed by calcination at 1350 °C for 6 hours. Na- γ - Al_2O_3 (sodium dispersed at the surface of γ - Al_2O_3) with a molar ratio of Na : Al = 1 : 15 was synthesized by wet impregnation of a solution of NaNO_3 (purity > 99 wt%) onto γ - Al_2O_3 . The material was dried at 100 °C in an oven overnight, followed by calcination at 900 °C for 2 h. In addition, commercially available α - Al_2O_3 (Alfa Aesar, aluminum oxide, α -phase, 99.9% metal basis) and γ - Al_2O_3 (Alfa Aesar, aluminum oxide, γ -phase, 99.98% metal basis) were utilized as reference materials. The XRD pattern of the references Na- β - Al_2O_3 , Na- γ - Al_2O_3 , α - Al_2O_3 and γ - Al_2O_3 are provided in Fig. S1.† All of the materials were exposed to ambient conditions before characterization. Thus, ambient humidity likely hydrated the surface of all studied oxygen carriers and references, and possibly also the interlayers in the case of Na- β - Al_2O_3 .

Characterization of the oxygen carriers

The crystalline phases of the calcined and cycled oxygen carriers were studied by XRD, using a PANalytical Empyrean X-ray powder diffractometer, equipped with a X'Celerator Scientific ultra-fast line detector and Bragg–Brentano HD incident beam optics using Cu K_α radiation (45 kV and 40 mA). A secondary monochromator was employed to suppress unwanted fluorescence originating from iron. Patterns were collected in the range of $2\theta = 5\text{--}90^\circ$, with a step size of 0.016° s^{-1} and a total acquisition time of 4 h. Rietveld refinements were performed using FullProf software.⁴¹

The local structure of the materials was characterized by XAS at the Fe, Na and Al K-edges. The Na K-edge and Al K-edge XAS measurements were carried out at the Phoenix II, elliptical undulator beamline at the Swiss Light Source (SLS) at the Paul Scherrer Institute (PSI), Switzerland. In a typical experiment a small quantity of material was pressed onto an indium foil and fixed to a copper plate.⁴² XAS measurements were performed in fluorescence mode. The X-ray fluorescence signal was detected using a 1-element Si-drift diode detector SDD (Ketek, Germany). Total electron yield was also collected in the case of Al K-edge measurements. In samples with a high content of absorbing atoms, *i.e.* non-diluted and not thin enough samples, the fluorescence detected XAS signal was corrected due to self-absorption. The current of the incoming beam (I_0) was measured using the total electron yield signal from a 0.5 µm thin polyester foil that was coated with a 50 nm thick layer of nickel. The beam passed through this foil approximately 1 m upstream of the sample in a vacuum chamber held at $\sim 10^{-6}$ mbar. Self-absorption correction in the Al K-edge spectra was applied. The Fe K-edge XAS spectra were collected at the BM31 beamline at the ESRF, Grenoble, France. The samples were ground, mixed with cellulose to optimize for X-ray absorption and pelletized. The data were collected in transmission mode using a Si(111) double crystal monochromator. Post-processing, self-absorption correction and analysis of the XAS data were performed using the Demeter 0.9.20 software package.⁴³

High-resolution field emission scanning electron microscopy (Zeiss ULTRA 55 plus) was employed to visualize the surface morphology of the oxygen carriers before and after cyclic redox tests. Furthermore, elemental mapping of the synthesized materials was achieved *via* a Leo Gemini 1530 SEM equipped with an energy dispersive X-ray spectrometer (EDX). A FEI Talos F200X operated at 200 kV was used in both transmission electron microscopy (TEM) and scanning TEM (STEM) modes, with a probe size of approximately 0.8 nm. The instrument is equipped with SuperX EDX comprising four SDD detectors. The STEM/EDX analyses were complemented with atomic number sensitive, high angle annular dark field (HAADF) STEM.

The surface area as well as the pore size distribution of the calcined oxygen carriers were determined using a Quantachrome NOVA 4000e N_2 adsorption analyser. The samples were degassed at 300 °C for two hours prior to the acquisition of the N_2 isotherms. The Brunauer–Emmett–Teller (BET)⁴⁴ and Barrett–Joyner–Halenda (BJH)⁴⁵ models were used to calculate, respectively, the surface area and the pore size distribution of the materials.

Redox performance

Cyclic redox experiments were performed in a packed bed reactor, as described in detail in a previous study.²³ The operating temperature was 800 °C to ensure a sufficiently high reduction rate allowing for a full reduction of Fe_2O_3 to Fe in the set time. A typical redox cycle consists of the following steps: (i) reduction in CO (10 vol% CO in N_2) for 15 minutes (1.5 L min^{-1}), (ii) purging with N_2 (1.5 L min^{-1}) for 1 minute, (iii)



oxidation of the reduced oxygen carrier with steam (23 vol% H₂O in N₂) for 7 minutes (1.94 L min⁻¹), (iv) purging with N₂ (1.5 L min⁻¹) for 1 minute, and (v) oxidation with 5 vol% O₂ in N₂ (2 L min⁻¹) for 5 minutes.

Results and discussion

First, we discuss the cyclic redox behaviour of the synthesized oxygen carriers to determine the effect of the addition of sodium on the redox performance of the materials. Subsequently, we probe in detail the structure of the oxygen carriers in the calcined stated and after exposure to 15 redox cycles to establish structure–performance correlations.

Cyclic redox performance

The cyclic redox performance of the oxygen carriers was assessed over 15 redox cycles in a packed bed reactor at 800 °C. In each cycle, the oxygen carriers were reduced in CO (10 vol% CO in N₂) and oxidized first in H₂O (23 vol% H₂O in N₂) and in a second step in O₂ (5 vol% O₂ in N₂). The concentration profiles of the off gases for the different oxygen carriers during redox cycling are given in Fig. S2.† For each cycle, the H₂ yield during steam oxidation was calculated by integrating the molar flow-rate of H₂ produced (obtained from off-gas concentration profiles) with respect to time by using eqn (7):²¹

$$\dot{N}_{\text{H}_2} = \dot{N}_{\text{N}_2} \times \int \frac{y_{\text{H}_2}}{1 - y_{\text{H}_2}} dt \quad (7)$$

where \dot{N}_{H_2} is the number of moles of H₂ produced, \dot{N}_{N_2} is the molar flow rate of N₂, and y_{H_2} is mole fraction of H₂ in the gas leaving the packed bed.

The H₂ yield expressed as mmol H₂ per g of oxygen carrier as a function of cycle number is given in Fig. 1. The H₂ yield of FeAl decreased rapidly over 15 cycles from 12.7 mmol H₂ per g oxygen carrier in the first cycle, to 11.1 mmol H₂ per g oxygen carrier in the fifth cycle and to 6 mmol H₂ per g oxygen carrier in the fifteenth cycle. The addition of sodium enhanced the redox stability of FeAlNa1 and increased the H₂ yield compared to FeAl; however, from the eighth redox cycle onwards also for this material the H₂ yield started to decrease. A more pronounced stabilization effect was observed in FeAlNa5. The H₂ yield of FeAlNa5 was stable over 15 redox cycles and was close to the theoretically expected value of 13.3 mmol g⁻¹ oxygen carrier. These results show that the introduction of sodium has a large impact on the cyclic behaviour of Al₂O₃ stabilized, Fe₂O₃-based oxygen carriers.

The effect of sodium on the reduction kinetics of iron oxide can be evaluated using the gas concentration profiles obtained in the first cycle. The concentration profiles of the off gases given in Fig. S3a,† show that FeAlNa1 and FeAlNa5 have very comparable reduction rates. The fractional conversion of the oxygen carriers tested are only marginally different in the first reduction step, which indicates that the presence of sodium does not affect appreciably the reduction kinetics of Fe₂O₃. The reduction characteristics of the oxygen carriers were assessed further by CO and H₂-TPR experiments (Fig. S4†). In the case of

steam oxidation, in the first cycle the conversion of FeAl was faster than the conversion of FeAlNa1 and FeAlNa5 indicating that the addition of sodium does not have a positive impact on oxidation kinetics (Fig. S5†). Over cycling, the water splitting kinetics decreased for the deactivating oxygen carriers (Fig. S6†). However, the overall oxidation duration of FeAlNa5 is fairly unaffected by the cycle number.

To obtain insight into the origin of the improved redox stability of FeAlNa1 and FeAlNa5 compared to FeAl, the morphological and structural characteristics of the calcined and cycled materials (15 cycles) were probed by XRD, XAS and STEM/EDX.

Structure of the calcined and cycled oxygen carriers by XRD and XAS

Calcined oxygen carriers. XRD analysis confirms that the main crystalline component in all of the calcined materials is hematite α -Fe₂O₃ (Fig. 2a and Table S2†). Additionally, α -Al₂O₃ (corundum) is observed in FeAl and FeAlNa1. In the case of FeAlNa5, there are also reflections due to α -Al₂O₃ observable; however, with a very weak intensity. In addition, FeAlNa5 contains a third phase, *i.e.* Na- β -Al₂O₃ ($P6_3/mmc$ space group, Fig. 2b).⁴⁶ Rietveld refinement allowed us to quantify the fraction of the crystalline phases in the oxygen carriers and to determine the cell parameters of these phases. The unit cell parameters of α -Fe₂O₃ and α -Al₂O₃ are reported in Table S2† and did not change (within the experimental error) upon the addition of sodium (Fig. 2 and Table S2†). The fact that the cell parameters are invariant with the addition of Na suggests that sodium is not incorporated into the crystal structures of α -Fe₂O₃ or α -Al₂O₃. The determined cell parameters of Na- β -Al₂O₃ ($a = b = 5.6385 \text{ \AA}$ and $c = 22.816 \text{ \AA}$) is in a good agreement with previous studies.^{46–48} The weight fractions of α -Al₂O₃ in the calcined materials were determined as 27, 23 and 3 wt% for FeAl and FeAlNa1 and FeAlNa5 respectively, *i.e.* the fraction of α -Al₂O₃ decreased with increasing Na content. For FeAl and FeAlNa1, α -Fe₂O₃ balanced the phase composition of the oxygen carriers, amounting to, respectively, 73 and 77 wt% α -Fe₂O₃. For FeAlNa5, the refined phase composition was 82 wt% α -Fe₂O₃, 15 wt% Na- β -Al₂O₃ and 3 wt% α -Al₂O₃. The presence of Na- β -Al₂O₃ in FeAlNa1 was not evidenced by XRD, yet this might be due to limitations of XRD in determining phases of low concentrations and/or poor crystallinity. To obtain further insight into the effect of the addition on sodium on the phase composition and structure of the oxygen carriers, we turned to an element specific technique X-ray technique, *i.e.* XAS at the Fe, Na and Al K-edges.

First, we analysed the local environment around iron. Fe K-edge XANES (X-ray absorption near edge structure) spectra of the calcined oxygen carriers are provided in Fig. 2d. The spectra of all of the oxygen carriers contain the same features as the α -Fe₂O₃ reference. The EXAFS (extended X-ray absorption fine structure) functions and the corresponding Fourier transforms (FT) are given in Fig. S7† and further confirm that the local environment around Fe corresponds to the local Fe environment in α -Fe₂O₃ in all three calcined materials. Hence, the XAS



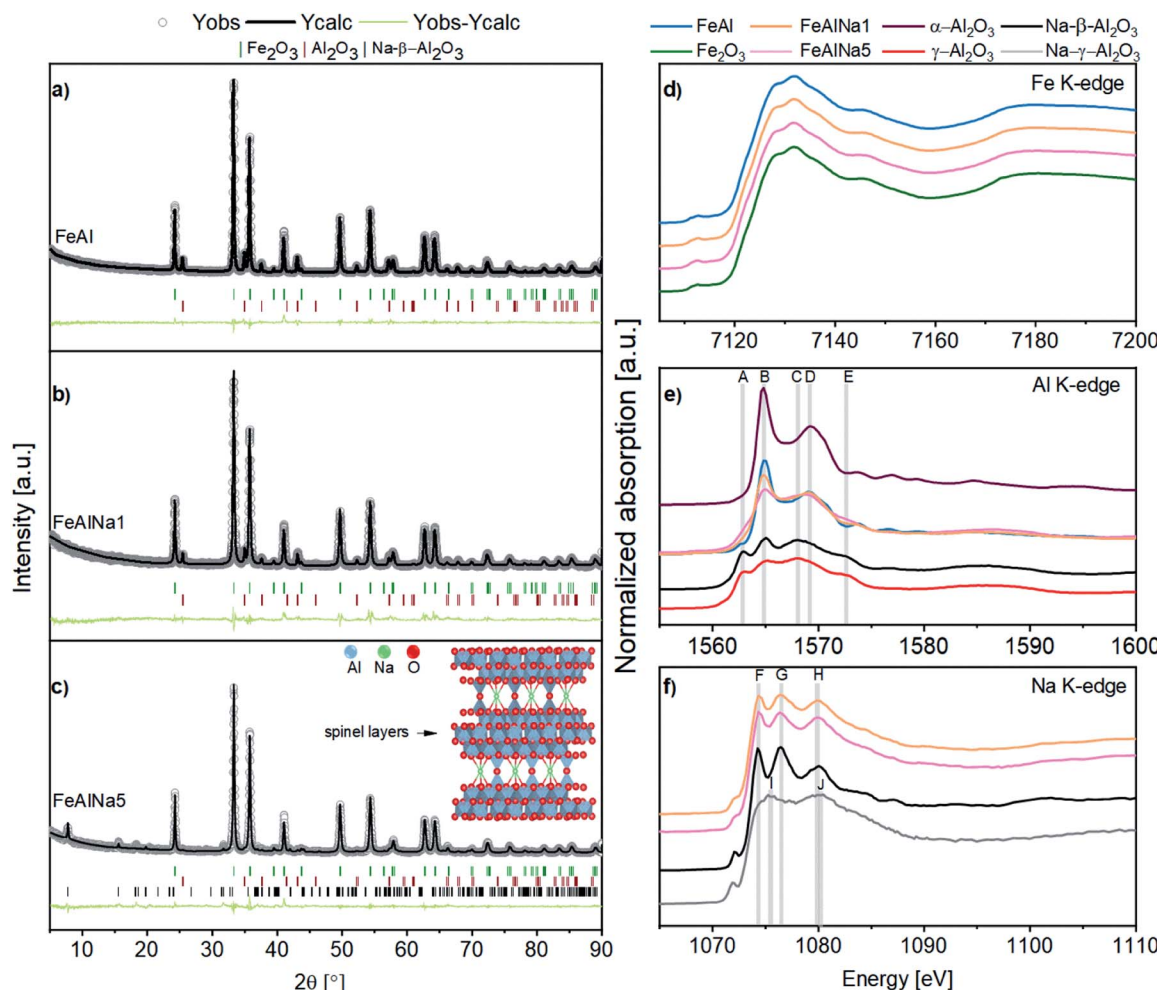


Fig. 2 (a)–(c) XRD patterns of the calcined oxygen carriers and the corresponding Rietveld refinements. The inset in (c) sketches the crystal structure of Na-β-Al₂O₃ containing layers of γ-alumina that are connected by bridging oxygen and sodium ions. XANES spectra at the (d) Fe K-edge, (e) Al K-edge, (f) Na K-edge of the calcined oxygen carriers and reference materials.

data confirm that the local environment of Fe is not affected by the presence of sodium. Importantly, it also shows that there is no formation of a solid solution or mixed oxide between Fe₂O₃ and Al₂O₃ upon calcination at 900 °C.

Fig. 2e displays the Al K-edge XANES spectra of the oxygen carriers and reference materials. To interpret these XANES data we will first discuss the XANES data of the reference materials α-Al₂O₃, γ-Al₂O₃ and Na-β-Al₂O₃. The crystal structure of α-Al₂O₃ is described by a hexagonal unit cell with Al in an octahedral coordination. The corresponding XANES spectrum (Fig. 2e) exhibits a doublet peak in the white-line region, with a sharp intense peak at 1565 eV (labelled as B), and a broader feature at 1568 eV (labelled as D), typical for Al in an octahedral coordination and in agreement with previously data.^{49,50} The reference γ-Al₂O₃ has a defect spinel type structure, in which Al atoms occupy both octahedral and tetrahedral sites.⁵¹ In the XANES spectrum of γ-Al₂O₃, features A, B, C and E are observed at 1563, 1565, 1568 and 1573 eV, respectively. In γ-Al₂O₃ feature B is considerably less intense than in α-Al₂O₃ and feature C has been attributed to tetrahedrally coordinated Al.^{52,53} Na-β-Al₂O₃ is a layered structure containing γ-Al₂O₃ layers that are linked by

sodium and oxygen atoms (inset in Fig. 2c).^{54,55} The fact that the Al K-edge XANES spectrum of Na-β-Al₂O₃ exhibits similar features as γ-Al₂O₃ confirms the presence of γ-Al₂O₃ layers in Na-β-Al₂O₃.⁵⁴

Next, we investigate the Al environment in the three oxygen carriers. The Al K-edge XANES spectrum of FeAl shows features B and D, indicating that Al³⁺ is in an octahedral coordination similar to α-Al₂O₃,⁴⁹ in line with XRD. With increasing sodium content, the intensity of feature B decreases, which implies that the fraction of α-Al₂O₃ in the material decreases with increasing sodium content. In agreement with our previous XRD analysis is the fact that the Al K-edge XANES spectrum of FeAlNa1 is dominated by features due to α-Al₂O₃. On the other hand, in FeAlNa5 features A, C and E are prominent which is indicative of the presence of spinel-type γ-Al₂O₃ or Na-β-Al₂O₃ (according to XRD). Features A, C and E are also present in FeAlNa1, but with a considerably lower intensity. Hence, our XANES results indicate that FeAlNa1 and FeAlNa5 contain a mixture of α-Al₂O₃ and a spinel-type Al₂O₃ phase. While α-Al₂O₃ is the main Al-based phase in FeAlNa1, Na-β-Al₂O₃ (or γ-Al₂O₃) is the main Al-containing phase in FeAlNa5. Na-β-Al₂O₃ and γ-Al₂O₃ share



the same Al K-edge features, yet combining the information of XRD and Na-Kedge XAS (*vide infra*), we assign the observed features to Na- β -Al₂O₃ rather than to γ -Al₂O₃. Lastly, we assess the Na environment in the oxygen carriers and reference materials. The Na K-edge XANES spectrum of Na- β -Al₂O₃ exhibits three main peaks labelled as F, G and H, located at 1074, 1076 and 1080 eV, respectively (Fig. 2f). To the best of our knowledge, this is the first experimentally collected Na K-edge spectrum of Na- γ -Al₂O₃ (*i.e.* the reference material prepared by wet impregnation of a solution of NaNO₃ onto γ -Al₂O₃) shows features different to Na- β -Al₂O₃ and are labelled I (1075 eV) and J (1080 eV) (Fig. S8†). These Na K-edge XANES features of Na- γ -Al₂O₃ are assigned to Na ions dispersed on the surface of γ -Al₂O₃ (in a solvated state).⁵⁵ Thus, using Na K-edge XANES we can distinguish between two different Na environments: (i) a Na- β -Al₂O₃ like environment, *i.e.* Na that is located between layers of γ -Al₂O₃ layers (ordered) and (ii) a Na- γ -Al₂O₃ like environment in which Na is located on the surface of γ -Al₂O₃ (surface Na⁺). The Na K-edge XANES spectra of FeAlNa1 and FeAlNa5 exhibit features F, G and H at, respectively 1074.4 eV (A), 1076.4 eV (B) and 1080.2 eV (C), suggesting a similar Na local environment in these two calcined oxygen carriers as in Na- β -Al₂O₃ (Fig. 2f). The presence of Na- β -Al₂O₃ in FeAlNa5 aligns with XRD results. The absence of diffraction peaks due to Na- β -Al₂O₃ in FeAlNa1 is possibly linked to its small quantity in FeAlNa1. However, we noticed

that the features F, G and H in the Na K-edge XANES spectra of FeAlNa1 and FeAlNa5 are less intense compared to the reference Na- β -Al₂O₃. This is possibly due to the presence of two different Na environments in the calcined oxygen carriers. This observation led us to propose that the Na K-edge XANES spectra of the oxygen carriers can be fitted by a linear combination of Na in an environment of Na- β -Al₂O₃ and surface Na⁺ in the form of Na- γ -Al₂O₃. Indeed, linear combination fitting yielded Na to be *ca.* 60% in a Na- β -Al₂O₃ environment and 40% in a Na- γ -Al₂O₃ type environment in both FeAlNa1 and FeAlNa5 (Fig. S9†).

Cycled oxygen carriers. To probe in depth the effect of sodium-containing phases on the redox stability of the Fe₂O₃-Al₂O₃ system the structures of the oxygen carriers that have undergone 15 redox cycles were also characterized by XRD and XAS. The cycled oxygen carriers were analysed in their reduced state as it has been argued that the presence of sodium hinders the formation of inactive hercynite during reduction.^{10,22,26}

The cycled materials (labelled with _cyc) exhibit dominant Bragg reflections due to fcc-Fe (Fig. 3a). However, the presence of magnetite (Fe₃O₄), wuestite-FeO (only in FeAl) and hercynite (spinel FeAl₂O₄) in FeAl_cyc and FeAlNa1_cyc points to an incomplete reduction. Importantly, the XRD pattern of FeAlNa5_cyc does not show peaks due to FeAl₂O₄, but peaks due to Na- β -Al₂O₃ (Fig. 3a), indicating that Na- β -Al₂O₃ is stable under redox conditions. The XANES spectra and FT-EXAFS functions of the three cycled oxygen carriers are shown in Fig. 3 and S10,† respectively.

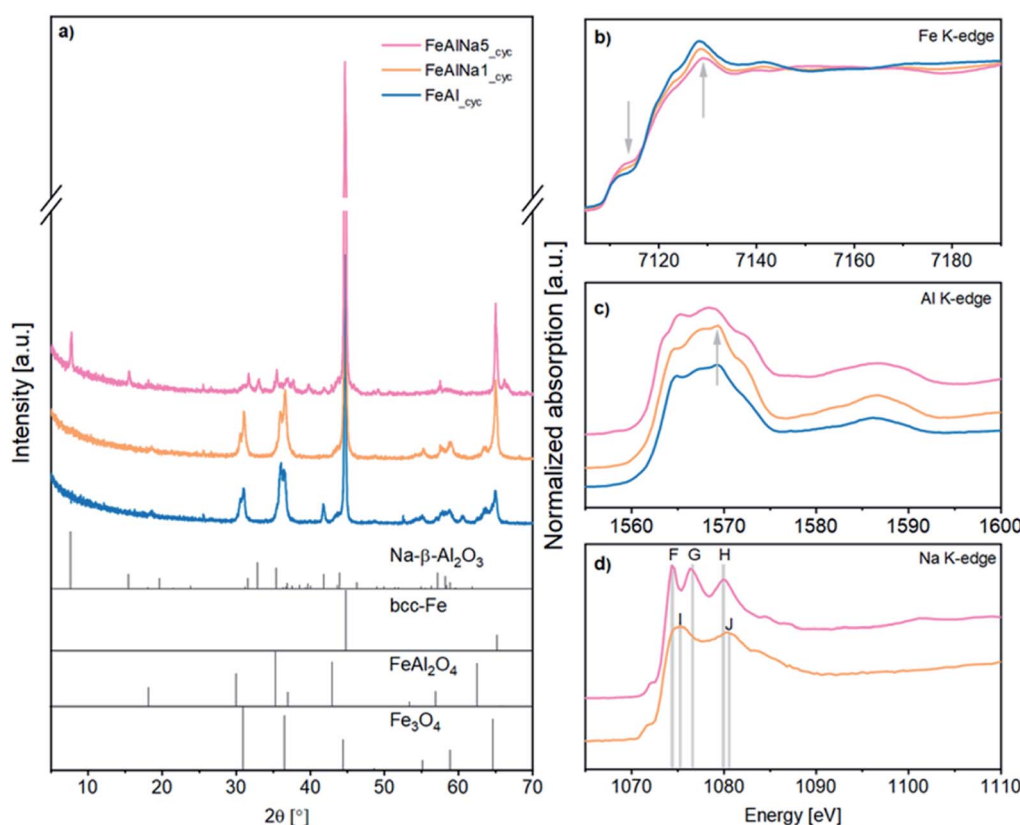


Fig. 3 (a) XRD patterns of the cycled oxygen carriers (15 redox cycles, reduction step) together with simulated diffraction patterns of the reference materials. XANES spectra at the (b) Fe K-edge (the arrows show the direction of change), (c) Al K-edge (the arrows point to distinct features in FeAlNa_{cyc} and FeAlNa_{5cyc}); and (d) Na K-edge of the cycled materials.



From the increase in the intensity of the white line it is clear that the degree of reduction followed the order $\text{FeAl}_{\text{cyc}} < \text{FeAlNa1}_{\text{cyc}} < \text{FeAlNa5}_{\text{cyc}}$. The Fe K-edge XANES spectra (Fig. 3b) of the oxygen carriers were fitted by a linear combination of an Fe foil, FeO and FeAl_2O_4 and yielded 48, 79 and 94 wt% metallic Fe^0 in, respectively, FeAl_{cyc} , $\text{FeAlNa1}_{\text{cyc}}$ and $\text{FeAlNa5}_{\text{cyc}}$. These results confirm that in FeAlNa5 the formation of FeAl_2O_4 during reduction is hindered and iron oxide can be reduced almost completely over 15 redox cycles. To some extent, there is also a stabilization effect in FeAlNa1 , yet the formation of FeAl_2O_4 could not be avoided fully. This is in line with the drop in the hydrogen yield of FeAlNa1 with cycle number.

Turning to the analysis of the Al K-edge XANES data of the cycled oxygen carriers, we did not observe any signatures due to $\alpha\text{-Al}_2\text{O}_3$ in any of the cycled oxygen carriers, instead features characteristic of spinel type phases are present. The Al K-edge XANES spectrum of $\text{FeAlNa5}_{\text{cyc}}$ (Fig. 3c) shows the same characteristic features as the $\text{Na}\text{-}\beta\text{-Al}_2\text{O}_3$ reference (Fig. 2e). This indicates that during redox cycling the small fraction of $\alpha\text{-Al}_2\text{O}_3$ that was initially present in calcined FeAlNa5 transforms fully to $\text{Na}\text{-}\beta\text{-Al}_2\text{O}_3$. Comparing the spectrum of $\text{FeAlNa5}_{\text{cyc}}$ with the spectra of FeAl_{cyc} and $\text{FeAlNa1}_{\text{cyc}}$ revealed a more intense feature at *ca.* 1569.6 eV for FeAl_{cyc} and $\text{FeAlNa1}_{\text{cyc}}$ (marked with an arrow in Fig. 3c). This feature can be attributed to the substitution of Al sites by Fe in a spinel structure in analogy to the spinel MgAl_2O_4 ⁵² which is isostructural to FeAl_2O_4 . Hence, consolidating with our XRD and Fe K-edge XAS results, the feature at 1569.6 eV in the Al K-edge XANES spectra of FeAl_{cyc} and $\text{FeAlNa1}_{\text{cyc}}$ is attributed to the formation of FeAl_2O_4 .

The Na K-edge XANES spectra of the cycled materials are shown in Fig. 3d. We observe that in $\text{FeAlNa5}_{\text{cyc}}$ the local environment of Na in the form of $\text{Na}\text{-}\beta\text{-Al}_2\text{O}_3$ is preserved during redox cycling. This is evidenced by the presence of the three features F, G and H in $\text{FeAlNa5}_{\text{cyc}}$. Linear combination fitting of the spectrum of $\text{FeAlNa5}_{\text{cyc}}$ yields 71% of Na in a $\text{Na}\text{-}\beta\text{-Al}_2\text{O}_3$ framework and 29% of Na in the form of surface Na ($\text{Na}\text{-}\gamma\text{-Al}_2\text{O}_3$ type). Hence, the fraction of Na in a $\text{Na}\text{-}\beta\text{-Al}_2\text{O}_3$ -type environment in FeAlNa5 increases with redox cycling, in line with Al K-edge XANES analysis. On the other hand, the Na K-edge XANES spectrum of $\text{FeAlNa1}_{\text{cyc}}$ exhibits, compared to FeAlNa5 , a different change in the Na environmental with redox cycling. The three sharp features (labelled F, G and H) in calcined FeAlNa1 are not detected in $\text{FeAlNa1}_{\text{cyc}}$ (Fig. S11†). Instead a broader doublet (features I and J) at 1075 and 1080.5 eV appears after redox cycling, indicative that $\text{FeAlNa1}_{\text{cyc}}$ closely resembles the spectrum of the $\text{Na}\text{-}\gamma\text{-Al}_2\text{O}_3$ reference. This change in the local environment of Na upon redox cycling, indicates that in FeAlNa1 Na is initially present in a $\text{Na}\text{-}\beta\text{-Al}_2\text{O}_3$ -like environment (in the layered structure), but migrates and disperses on the material's surface during redox cycling.

Morphology and elemental mapping of the calcined and cycled carriers

The morphology of the freshly calcined oxygen carriers, as probed by electron microscopy is affected only marginally by the addition of sodium (Fig. S12†). The calcined oxygen carriers

FeAl , FeAlNa1 and FeAlNa5 were composed of particles with an average grain size of $\sim 100 \pm 20$ nm (based on the analysis of 50 particles). The particle size of Fe_2O_3 , calculated using STEM-EDX maps of the calcined oxygen carriers (Fig. S13†), was in the range of 80–120 nm for the oxygen carriers tested (119 ± 33 nm, 135 ± 36 nm and 87 ± 40 nm for FeAl , FeAlNa1 and FeAlNa5 , respectively). The weight composition of the materials as determined by SEM/EDX (Table S1†) are in good agreement with the nominal compositions of the oxygen carriers. The elemental mapping of the oxygen carriers revealed that the sol-gel synthesis led to a high dispersion of Fe, Na and Al, indicating that the different phases were highly dispersed in the materials (Fig. S14†). The calcined oxygen carriers FeAl , FeAlNa1 and FeAlNa5 have similar BET surface areas and BJH pore volumes (Table S1†).

HAADF-STEM images and the corresponding EDX maps of Fe, Al and Na are given in Fig. 4. In the calcined materials FeAl , FeAlNa1 , and FeAlNa5 , discrete Fe_2O_3 - and Al_2O_3 -rich particles are formed, and Na is distributed evenly in FeAlNa1 . In FeAlNa5 , the EDX signals of Al and Na overlap, which is in line with the outcome of the XRD and XAS analysis (Fig. 2) pointing to the formation of a $\text{Na}\text{-}\beta\text{-Al}_2\text{O}_3$ phase. Similarly, the EDX maps of FeAl_{cyc} and $\text{FeAlNa1}_{\text{cyc}}$ show overlapping signals of Fe and Al, which are in agreement with the formation of the spinel FeAl_2O_4 as determined by XRD and XAS. No such overlap is observed in $\text{FeAlNa5}_{\text{cyc}}$, which features discrete Al- and Fe-rich particles. Furthermore, the overlapping signals of Na and Al in $\text{FeAlNa5}_{\text{cyc}}$ provide further evidence for the formation of $\text{Na}\text{-}\beta\text{-Al}_2\text{O}_3$ as determined by the XRD and XAS analyses.

Structure–performance relationships

Combining the results of the cyclic redox tests, with our XRD, XAS and HAADF-STEM-EDX analyses we can propose the following structure–performance correlations. The reaction of $\alpha\text{-Al}_2\text{O}_3$ with Fe/FeO_x during redox cycling leads to the formation of (inactive) FeAl_2O_4 that in turn correlates with a rapid decay in the H_2 yield in FeAl . The high redox stability of FeAlNa5 correlates with the formation of $\text{Na}\text{-}\beta\text{-Al}_2\text{O}_3$ and the absence of $\alpha\text{-Al}_2\text{O}_3$ in this oxygen carrier. The formation of $\text{Na}\text{-}\beta\text{-Al}_2\text{O}_3$ in FeAlNa5 hinders effectively the formation of FeAl_2O_4 during repeated redox cycles, leading in turn to a material with a stable hydrogen yield. The $\text{Na}\text{-}\beta\text{-Al}_2\text{O}_3$ phase is stable at reductive and oxidative environments and is highly dispersed within the Fe/ FeO_x matrix. The oxygen carrier with a lower Na content, *i.e.* FeAlNa1 , shows a dominating presence of $\alpha\text{-Al}_2\text{O}_3$ and a small fraction of $\text{Na}\text{-}\beta\text{-Al}_2\text{O}_3$ initially freshly calcined state. Such a phase composition can only partially stabilize the oxygen carrier. Indeed, in FeAlNa1 , Na is initially present in two environments *i.e.* as $\text{Na}\text{-}\beta\text{-Al}_2\text{O}_3$ and dispersed as surface Na. During the redox cycling of FeAlNa1 , all of the $\alpha\text{-Al}_2\text{O}_3$ reacts with FeO_x forming FeAl_2O_4 , while sodium is found in a non-crystalline form (dispersed at the surface of the particle). A schematic representation of the phase evolution during redox cycling is given in Fig. S15.† Therefore, our study points to the critical role of the layered $\text{Na}\text{-}\beta\text{-Al}_2\text{O}_3$ phase in stabilizing the hydrogen yield of Al_2O_3 -stabilized, Fe_2O_3 based oxygen carriers.



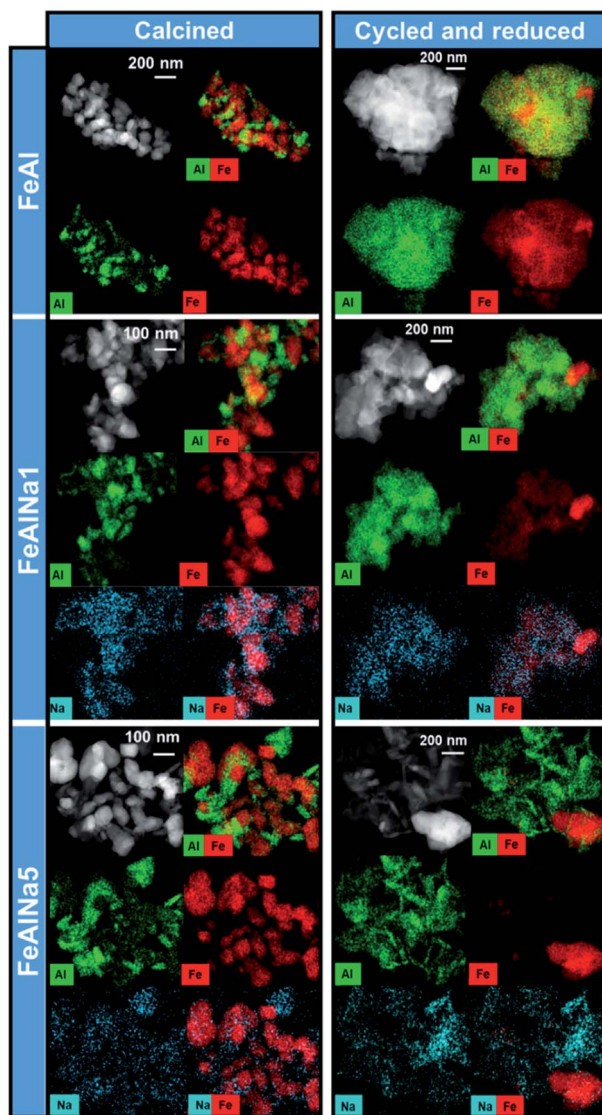


Fig. 4 HAADF images and elemental maps (STEM-EDX) of the calcined oxygen carriers and after cycling experiments (15 cycles, reduction step).

Conclusions

In this work, we probe the effect of the addition of sodium to Fe_2O_3 – Al_2O_3 -based oxygen carriers, on their redox stability, phase composition and phase dynamics over redox cycles. Application of XRD, XAS at the Al, Na and Fe K-edges and STEM/EDX to the freshly calcined and cycled materials allowed us to draw the following conclusions:

(i) $\alpha\text{-Al}_2\text{O}_3$ reacts with Fe/FeO_x during redox cycling leading to the formation of FeAl_2O_4 ; the formation of which correlates directly with the rapid decrease in the H_2 yield of an oxygen carrier.

(ii) Depending on the loading of sodium in the oxygen carrier, sodium can be found in a crystalline $\text{Na}\text{-}\beta\text{-Al}_2\text{O}_3$ phase or at the surfaces of the particles.

(iii) Na in the environmental of the layered structure $\text{Na}\text{-}\beta\text{-Al}_2\text{O}_3$ effectively stabilizes the redox performance of an oxygen carrier, while surface sodium cannot prevent fully material deactivation.

This work, demonstrates how probing of the local and average structure, such as multi edge XAS analysis in combination with XRD and electron microscopy allows for the formulation of structure–performance correlations. In addition, this work showcases the application of XAS in the tender X-ray region (Na and Al K-edges) that have not been investigated extensively particularly in the field of chemical looping and can, therefore, be of interest to the broader functional materials community. Our study brings fundamental understanding of the role of $\text{Na}\text{-}\beta\text{-Al}_2\text{O}_3$ for the stabilization of Fe_2O_3 -based oxygen carriers. Nonetheless, further studies that explore different reducing gases (such as CH_4), operation temperatures and long-term stability (>100 cycles) are required.

Conflicts of interest

There are no conflicts to declare.

Acknowledgements

The authors would like to acknowledge the Swiss National Science Foundation (406640_136707) and the Swiss Office of Energy (BFE, SI/500652) for financial support. This project has received partial funding from the European Union's Horizon 2020 research and innovation program (grant agreement No. 800419). This publication was created as part of NCCR Catalysis, a National Centre of Competence in Research funded by the Swiss National Science Foundation. We also thank Scientific Centre for Optical and Electron Microscopy (ScopeM) for providing training and access to scanning electron microscopes. The authors are grateful to the Swiss Light Source (SLS) at the Paul Scherrer Institute (Villigen, Switzerland), for providing beamtime at the PHOENIX beamline, and to the European Synchrotron Facility (ESRF) and the Swiss-Norwegian beamline (SNBL at ESRF) for providing beamtime for XAS measurements. We thank Dr Felix Donat for the insightful discussions on thermodynamic analysis.

Notes and references

- BP, *Energy Outlook 2017 Edition*, 2017.
- IEA, *Technology Roadmap: Hydrogen and Fuel Cells*, 2015.
- J. A. Turner, *Science*, 2004, **305**, 972–974.
- M. Zerta, P. R. Schmidt, C. Stiller and H. Landinger, *Int. J. Hydrogen Energy*, 2008, **33**, 3021–3025.
- T. V. Choudhary and D. Goodman, *Catal. Today*, 2002, **77**, 65–78.
- G. Postole and A. Auroux, *Int. J. Hydrogen Energy*, 2011, **36**, 6817–6825.
- C. Bohn, J. Cleeton, C. Müller, S. Chuang, S. Scott and J. Dennis, *Energy Fuels*, 2010, **24**, 4025–4033.
- A. Thursfield, A. Murugan, R. Franca and I. S. Metcalfe, *Energy Environ. Sci.*, 2012, **5**, 7421–7459.



9 Q. Zafar, T. Mattisson and B. Gevert, *Ind. Eng. Chem. Res.*, 2005, **44**, 3485–3496.

10 P. R. Kidambi, J. P. E. Cleeton, S. A. Scott, J. S. Dennis and C. D. Bohn, *Energy Fuels*, 2012, **26**, 603–617.

11 J. R. Scheffe, M. D. Allendorf, E. N. Coker, B. W. Jacobs, A. H. McDaniel and A. W. Weimer, *Chem. Mater.*, 2011, **23**, 2030–2038.

12 R. D. Solunke and G. Veser, *Ind. Eng. Chem. Res.*, 2010, **49**, 11037–11044.

13 N. S. Yüzbasi, P. M. Abdala, Q. Imtiaz, S. M. Kim, A. M. Kierzkowska, A. Armutlulu, W. van Beek and C. R. Müller, *Phys. Chem. Chem. Phys.*, 2018, **20**, 12736–12745.

14 L.-S. Fan and F. Li, *Ind. Eng. Chem. Res.*, 2010, **49**, 10200–10211.

15 G. Voitic and V. Hacker, *RSC Adv.*, 2016, **6**, 98267–98296.

16 M. Rydén and M. Arjmand, *Int. J. Hydrogen Energy*, 2012, **37**, 4843–4854.

17 C. D. Bohn, C. R. Müller, J. P. Cleeton, A. N. Hayhurst, J. F. Davidson, S. A. Scott and J. S. Dennis, *Ind. Eng. Chem. Res.*, 2008, **47**, 7623–7630.

18 J. P. E. Cleeton, C. D. Bohn, C. R. Müller, J. S. Dennis and S. A. Scott, *Int. J. Hydrogen Energy*, 2009, **34**, 1–12.

19 D. Hosseini, F. Donat, S. M. Kim, L. Bernard, A. M. Kierzkowska and C. R. Müller, *ACS Appl. Energy Mater.*, 2018, **1**, 1294–1303.

20 W.-C. Huang, Y.-L. Kuo, P.-C. Su, Y.-H. Tseng, H.-Y. Lee and Y. Ku, *Chem. Eng. J.*, 2018, **334**, 2079–2087.

21 Q. Imtiaz, N. S. Yüzbasi, P. M. Abdala, A. M. Kierzkowska, W. van Beek, M. Broda and C. R. Müller, *J. Mater. Chem. A*, 2016, **4**, 113–123.

22 A. Kierzkowska, C. Bohn, S. Scott, J. Cleeton, J. Dennis and C. Muller, *Ind. Eng. Chem. Res.*, 2010, **49**, 5383–5391.

23 W. Liu, J. S. Dennis and S. A. Scott, *Ind. Eng. Chem. Res.*, 2012, **51**, 16597–16609.

24 C. Müller, C. Bohn, Q. Song, S. Scott and J. Dennis, *Chem. Eng. J.*, 2011, **166**, 1052–1060.

25 J. B. Yang, N. S. Cai and Z. S. Li, *Energy Fuels*, 2008, **22**, 2570–2579.

26 N. S. Yüzbasi, A. Kierzkowska and C. Müller, *Energy Procedia*, 2017, **114**, 436–445.

27 N. S. Yüzbasi, A. M. Kierzkowska, Q. Imtiaz, P. M. Abdala, A. Kurlov, J. L. M. Rupp and C. R. Müller, *J. Phys. Chem. C*, 2016, **120**, 18977–18985.

28 Z. Ma, S. Zhang and R. Xiao, *Energy Convers. Manage.*, 2019, **188**, 429–437.

29 M. Ishida, K. Takeshita, K. Suzuki and T. Ohba, *Energy Fuels*, 2005, **19**, 2514–2518.

30 C. Chung, L. Qin, V. Shah and L.-S. Fan, *Energy Environ. Sci.*, 2017, **10**, 2318–2323.

31 W. Liu, M. Ismail, M. T. Dunstan, W. Hu, Z. Zhang, P. S. Fennell, S. A. Scott and J. S. Dennis, *RSC Adv.*, 2015, **5**, 1759–1771.

32 M. Arjmand, A.-M. Azad, H. Leion, T. Mattisson and A. Lyngfelt, *Ind. Eng. Chem. Res.*, 2012, **51**, 13924–13934.

33 J. Adanez, A. Abad, F. Garcia-Labiano, P. Gayan and L. F. de Diego, *Prog. Energy Combust. Sci.*, 2012, **38**, 215–282.

34 Q. Imtiaz, P. M. Abdala, A. M. Kierzkowska, W. Van Beek, S. Schweiger, J. L. Rupp and C. R. Müller, *Phys. Chem. Chem. Phys.*, 2016, **18**, 12278–12288.

35 A. Turnock and H. Eugster, *J. Petrol.*, 1962, **3**, 533–565.

36 K. J. Warren, J. T. Tran and A. W. Weimer, *Energy Environ. Sci.*, 2022, **15**, 806–821.

37 C. L. Muhich, B. W. Evanko, K. C. Weston, P. Lichty, X. Liang, J. Martinek, C. B. Musgrave and A. W. Weimer, *Science*, 2013, **341**, 540–542.

38 C. L. Muhich, B. D. Ehrhart, V. A. Witte, S. L. Miller, E. N. Coker, C. B. Musgrave and A. W. Weimer, *Energy Environ. Sci.*, 2015, **8**, 3687–3699.

39 Q. Song, W. Liu, C. D. Bohn, R. N. Harper, E. Sivaniah, S. A. Scott and J. S. Dennis, *Energy Environ. Sci.*, 2013, **6**, 288–298.

40 L. Liu and M. R. Zachariah, *Energy Fuels*, 2013, **27**, 4977–4983.

41 J. Rodriguez-Carvajal, *Phys. B*, 1993, **192**, 55.

42 M. Galib, M. Baer, L. Skinner, C. Mundy, T. Huthwelker, G. Schenter, C. Benmore, N. Govind and J. L. Fulton, *J. Chem. Phys.*, 2017, **146**, 084504.

43 B. Ravel and M. Newville, *J. Synchrotron Radiat.*, 2005, **12**, 537–541.

44 S. Brunauer, P. H. Emmett and E. Teller, *J. Am. Chem. Soc.*, 1938, **60**, 309–319.

45 E. P. Barrett, L. G. Joyner and P. P. Halenda, *J. Am. Chem. Soc.*, 1951, **73**, 373–380.

46 N. Zhu, F. Guo, S. Yan, L. Chen and A. Li, *Acta Chim. Sin.*, 1992, **50**, 527–532.

47 W. A. England, A. J. Jacobson and B. C. Tofield, *Solid State Ionics*, 1982, **6**, 21–27.

48 C. Peters, M. Bettman, J. t. Moore and M. Glick, *Acta Crystallogr., Sect. B: Struct. Crystallogr. Cryst. Chem.*, 1971, **27**, 1826–1834.

49 A. Omegna, R. Prins and J. A. van Bokhoven, *J. Phys. Chem. B*, 2005, **109**, 9280–9283.

50 D. R. Neuville, L. Cormier, A.-M. Flank, V. Briois and D. Massiot, *Chem. Geol.*, 2004, **213**, 153–163.

51 R. Prins, *J. Catal.*, 2020, **392**, 336–346.

52 D. R. Neuville, D. De Ligny, L. Cormier, G. S. Henderson, J. Roux, A.-M. Flank and P. Lagarde, *Geochim. Cosmochim. Acta*, 2009, **73**, 3410–3422.

53 Y. Kato, K.-i. Shimizu, N. Matsushita, T. Yoshida, H. Yoshida, A. Satsuma and T. Hattori, *Phys. Chem. Chem. Phys.*, 2001, **3**, 1925–1929.

54 A. Marcelli, A. Mottana and G. Cibin, *J. Appl. Crystallogr.*, 2000, **33**, 234–242.

55 M. Digne, P. Raybaud, P. Sautet, D. Guillaume and H. Toulhoat, *Phys. Chem. Chem. Phys.*, 2007, **9**, 2577–2582.

